Fluorine production in intermediate-mass stars

N. Mowlavi * A. Jorissen † M. Arnould

Institut d'Astronomie et d'Astrophysique,
Université Libre de Bruxelles, C.P.226,
Boulevard du Triomphe,
B-1050 Bruxelles,
Belgium

Abstract

The ^{19}F production during the first dozen thermal pulses of AGB stars with masses M and metallicities Z ($M = 3\,\mathrm{M}_\odot$, $Z = 0.02$), ($M = 6\,\mathrm{M}_\odot$, $Z = 0.02$) and ($M = 3\,\mathrm{M}_\odot$, $Z = 0.001$) is investigated on grounds of detailed stellar models and of revised rates for $^{15}\mathrm{N}\,(\alpha\,,\gamma)\,^{19}\mathrm{F}$ and $^{18}\mathrm{O}(\alpha,\gamma)^{22}\mathrm{Ne}$. These calculations confirm an early expectation that ^{19}F *is* produced in AGB thermal pulses. They also enlarge substantially these previous results by showing that the variations of the level of ^{19}F production during the evolution is very sensitive to the maximum temperature reached at the base of the pulse. These variations are analyzed in detail, and are shown to result from a subtle balance between different nuclear effects (mainly ^{19}F production or destruction in a pulse, and ^{15}N synthesis during the interpulse), possibly superimposed on dilution effects in more or less extended pulse convective tongues.

Our calculations, as most others, do not predict the third dredge-up self-consistently. When parametrized, it appears that our models of intermediate-mass AGB stars are able to account only for the lowest ^{19}F overabundances observed in solar-metallicity MS, S and C stars. That conclusion is expected to hold true for low-mass stars when fluorine production results from secondary ^{13}C only. Massive AGB stars, on the other hand, are not expected to build up large surface F abundances. Therefore, the large fluorine overabundance reported for the super Li-rich star WZ Cas (where hot bottom burning is supposed to be operating) remains unexplained so far. Our results for the ($3\,\mathrm{M}_\odot$, $Z = 0.001$) star indicate that fluorine surface overabundances can also be expected in low-metallicity stars provided that third dredge-ups occur after the early cool pulses. The relative increase in the surface $^{19}\mathrm{F}/^{12}\mathrm{C}$ ratio is, however, lower in the low-metallicity than in the solar-metallicity star. No observations are reported yet for these stars, and are urgently called for.

Keywords: nuclear reactions – nucleosynthesis – abundances – stars: evolution – stars: AGB

*Present Address: Observatoire de Genève, CH-1290 Sauverny, Switzerland
†Research Associate, National Fund for Scientific Research (FNRS), Belgium

1 Introduction

Fluorine overabundances in giant stars of spectral types MS, S and C have been reported recently (Jorissen, Smith & Lambert 1992; Paper I). These observations reveal a progressive F enrichment of the envelope as the C/O ratio increases, reaching [F/O] ≈ 1.5 in some C stars. An independent indication of large F overabundances in carbon stars comes from the recent detection of AlF in the inner envelope of the dust-enshrouded carbon star IRC+10216 (Ziurys, Apponi & Phillips 1994). These observations shed light on the much debated question of the nucleosynthetic origin of ^{19}F. They clearly point towards thermal pulses as a likely site for its production.

The first quantitative proof that ^{19}F can indeed be produced in thermally pulsing AGB stars has been provided by Forestini et al. (1992; Paper II). However, this early investigation just considered the first 4 thermal pulses of a single (3 $M_\odot$, $Z = 0.03$) star. As a consequence, it left unanswered several important questions, like the dependence of the level of ^{19}F production on the stellar mass, metallicity, or pulse number.

The present paper aims at exploring some of these questions. It analyzes a dozen pulses in three stars of different masses and metallicities ($M = 3\,M_\odot$, $Z = 0.02$; $M = 6\,M_\odot$, $Z = 0.02$; $M = 3\,M_\odot$, $Z = 0.001$). Use is made of an improved code which follows more accurately the structural evolution of the AGB stars and the concomitant nucleosynthesis. It also updates some nuclear reaction data of importance in the study of the ^{19}F production. In particular, a more accurate rate (de Olivera et al. 1995) for the key reaction $^{15}\mathrm{N}(\alpha,\gamma)^{19}\mathrm{F}$ is adopted, as well as a recent re-evaluation (Giesen et al. 1994) of the $^{18}\mathrm{O}(\alpha,\gamma)^{22}\mathrm{Ne}$ rate. In addition, the surface fluorine enhancement due to the first and second dredge-ups is also investigated.

The nuclear transformations leading to the production of ^{19}F in thermal pulses are reviewed in Sect. 2. The evolution code and its key ingredients are briefly described in Sect. 3, while Sect. 4 presents our calculated ^{19}F abundances. Our expectations are confronted with the observational data in Sect. 5, and conclusions are drawn in Sect. 6

2 The nuclear transformations governing the ^{19}F production in thermal pulses

The reaction chain producing ^{19}F in thermal pulses has been identified in Paper II, and is displayed in Fig. 1. Its main characteristics may be summarized as follows:

(1) the main seeds for ^{19}F production are ^{13}C and ^{14}N left behind by the H-burning shell. The resulting relatively small amount of ^{13}C is the main factor that limits the amount of ^{19}F possibly produced in a thermal pulse. The efficiency of the ^{19}F synthesis in a pulse can be expressed as $(Y^*_{\rm out}(^{15}\mathrm{N})+Y^*_{\rm out}(^{19}\mathrm{F}))/Y_{\rm in}(^{13}\mathrm{C})$. In this ratio, $Y_{\rm in}(^{13}\mathrm{C})$ represents the abundance by number of ^{13}C injected in the pulse, and $Y^*_{\rm out}(^{15}\mathrm{N})$ and $Y^*_{\rm out}(^{19}\mathrm{F})$ are the abundances by number of ^{15}N and ^{19}F at the end of the pulse, assuming zero initial ^{19}F and ^{15}N abundances.

(2) the main loss of efficiency in the ^{19}F synthesis comes from the (n,γ) reactions, mainly on ^{56}Fe and heavier nuclei. They limit the occurrence of $^{14}\mathrm{N}\,(\mathrm{n}\,,\mathrm{p})\,^{14}\mathrm{C}$ and $^{26}\mathrm{Al}\,(\mathrm{n}\,,\mathrm{p})\,^{26}\mathrm{Mg}$ reactions, which are the main producers of the protons required for manufacturing ^{15}N, the ^{19}F progenitor[1].

[1]The role of ^{26}Al in enhancing the ^{19}F production in thermal pulses has been identified in Paper II. The

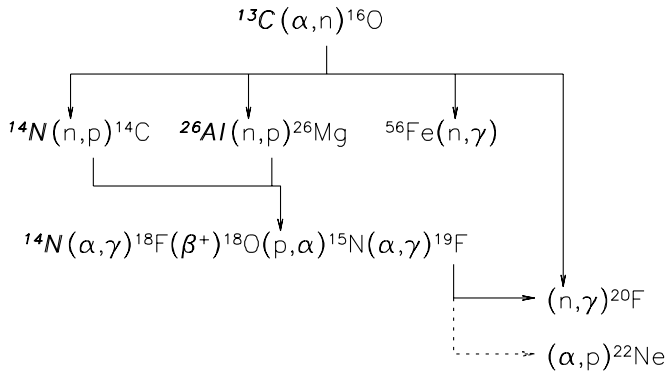

Figure 1: The chain of reactions producing ^{19}F in thermal pulse conditions. Bold italicized species are ashes from the H-burning shell. The most important (n,γ) capture competing with the indicated (n,p) reactions is $^{56}\mathrm{Fe}\,(\mathrm{n}\,,\gamma)$

(3) almost all the protons liberated as indicated above can lead to the production of ^{19}F if indeed the $^{18}\mathrm{O}\,(\mathrm{p}\,,\alpha)\,^{15}\mathrm{N}\,(\alpha,\gamma)^{19}\mathrm{F}$ chain develops. A necessary condition for this to occur is the availability of ^{18}O. Some ^{18}O might be inherited from previous pulses. As no interpulse ^{18}O burning is predicted by our models, this requires mainly that the duration $\Delta t_{\rm pulse}$ of these pulses be shorter than the destruction time scale of ^{18}O against α-capture. If this is not the case, no ^{18}O from former pulses can survive at the beginning of a pulse. In such conditions, and as $^{14}\mathrm{N}\,(\alpha\,,\gamma)\,^{18}\mathrm{F}\,(\beta^+)\,^{18}\mathrm{O}$ is slower than $^{13}\mathrm{C}\,(\alpha\,,\mathrm{n})\,^{16}\mathrm{O}$ for typical pulse temperatures, one would expect the neutrons to be liberated and captured by the heavy nuclides before any ^{18}O is made available. In this case, the reaction chain leading the synthesis of ^{19}F displayed in Fig. 1 would not operate.

In fact, the situation as it comes out of the detailed calculations to be reported in Sect. 4 is quite different. In reality, the nuclear sequence of Fig. 1 can still operate in a pulse *even if* that pulse does not inherit any ^{18}O from previous pulses. We refer to Sect. 4 for details.

(4) ^{19}F has the rather large Maxwellian-averaged neutron-capture cross section of 5.7 mb at 30 keV (Beer, Voss & Winters 1992). It has been checked that (i) $^{19}\mathrm{F}\,(\mathrm{n}\,,\gamma)\,^{20}\mathrm{F}$ has no influence on the neutron budget. This results from the fact that ^{14}N or ^{56}Fe are much more important neutron captors than ^{19}F; and (ii) $^{19}\mathrm{F}\,(\mathrm{n}\,,\gamma)\,^{20}\mathrm{F}$ could become a significant ^{19}F destruction channel only for much larger neutron fluences than the ones predicted by the models reported in this paper. In fact, if the larger neutron production would result from a primary ^{13}C reservoir, an *increased* ^{19}F production would also be obtained from the chain of transformations of Fig. 1, thus limiting the impact of $^{19}\mathrm{F}\,(\mathrm{n}\,,\gamma)\,^{20}\mathrm{F}$. The models reported in this paper do not consider such a possibility, which deserves further detailed studies.

(5) as shown in Fig. 1, $^{19}\mathrm{F}\,(\alpha\,,\mathrm{p})\,^{22}\mathrm{Ne}$ could destroy some of the produced ^{19}F if the corresponding destruction time scale, $\tau_\alpha(^{19}\mathrm{F})$, gets shorter than $\Delta t_{\rm pulse}$. This happens when the temperature at the base of the pulse exceeds typically $\sim 300\,10^6$ K. The ^{19}F production is therefore expected to be less efficient in the late AGB evolutionary stages, when the pulse temperatures are high.

H-burning shell of AGB stars is known to produce large amounts of ^{26}Al (Forestini et al. 1991)

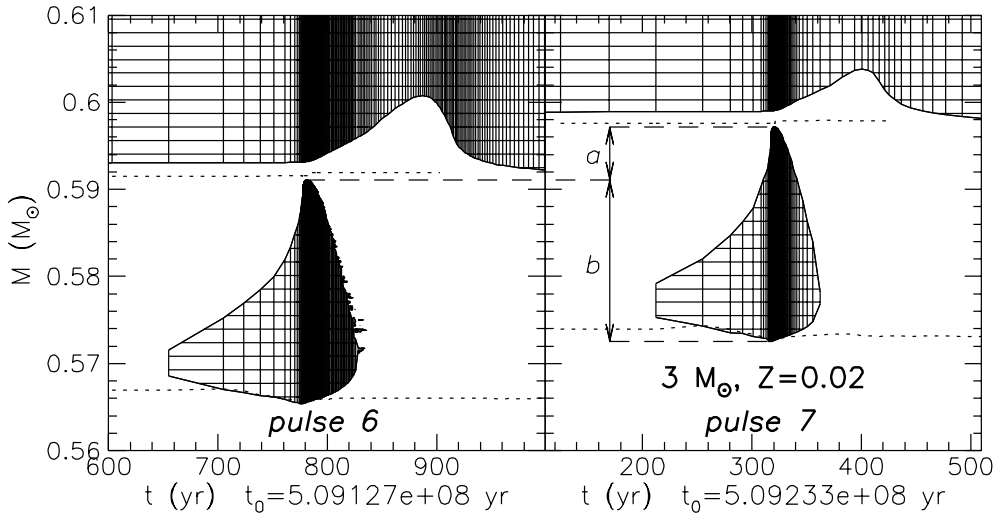

Figure 2: The 6th and 7th pulses of the 3 $M_\odot$, $Z = 0.02$ star. The scales are the same in both panels. Hatched regions correspond to convective zones. Each computed model is represented by a vertical line in the convective zones (horizontal lines have no special meaning). The short-dashed lines identify the location of maximum energy production in the H-burning (top) and He-burning (bottom) layers. Regions a and b as defined in the text are also indicated

Finally, it has to be noted that the ^{19}F synthesis in convective pulses involves species that may have nuclear lifetimes shorter than, or similar to, the convective mixing time scale. This situation is encountered for neutrons and protons. A proper treatment of the ^{19}F production may therefore require the use of an algorithm coupling nucleosynthesis and convective diffusion. This question will be addressed further in Sect. 4.

3 Key ingredients of the stellar evolution code

A new implicit stellar evolution code that differs in several ways from the one used in Paper II has been designed in order to follow accurately the evolution of the structurally very complex AGB stars (see Mowlavi 1995a for a full description of the code). Its new features significantly improve the numerical accuracy of the models, and avoid spurious numerical effects exhibited by the models of Paper II.

In particular, the algorithm defining the discrete mass zones is based on the structural equations, rather than on the relative variations of the dependent variables. This provides a better handle on the accuracy achieved on the structure[2]. Convective zones growing into regions of variable chemical composition have been modeled with great care. A special algorithm moreover ensures that composition discontinuities remain sharp as the star evolves, thus avoiding "numerical chemical diffusion" as encountered in the models of Paper II.

Each model is computed by iterating the nucleosynthesis + mixing and the structure calculations. Starting with an initial model at time t, taken identical to the model at time

[2]This structural accuracy is different from the relative precision required for the convergence of the Newton-Raphson solution of the structural equations. The latter easily reaches 10^{-5} in all our models.

$t - \Delta t$, where Δt is the time step between the two models, a first iteration is performed by calculating the nucleosynthesis + mixing, followed by the calculation of the structure through a Newton-Raphson method. A second iteration performs the nucleosynthesis + mixing on the last calculated structure, followed by a new calculation of the structure. The procedure goes on until the structure and the chemical distribution have converged. Two to three such iterations are usually sufficient. From the core helium-burning phase on, however, the number of iterations is limited to two, still providing a satisfactory accuracy within reasonable computer times. Rezoning is applied after each structure calculation in order to reach the required accuracy, and to predict the location of the convective boundaries to better than 10^{-5} $M_\odot$. Instantaneous mixing and concomitant homogeneous composition are assumed in the convective zones, except for nuclides with nuclear lifetimes $\tau_{\rm nuc}$ shorter than the convective mixing time scale $\tau_{\rm mix}$. More specifically, the nucleosynthesis is calculated in a one-zone approximation making use of an effective reaction rate obtained by averaging the reaction rate over the convective zone (see Prantzos, Arnould & Arcoragi 1987 for more details). When $\tau_{\rm nuc} < \tau_{\rm mix}$ for a given nuclide, its abundance must be computed separately in each layer. In practice, it is found that these nuclides (mainly neutrons, protons and sometimes ^{18}O) usually also satisfy the condition of local equilibrium between production and destruction, from which their abundance can easily be computed in each layer. This procedure is only applied to nuclides with $X \leq 10^{-15}$ in the convective zone (where X is the mass fraction), like neutrons and often protons. Species more abundant than $X = 10^{-15}$ or with $\tau_{\rm nuc} \sim \tau_{\rm mix}$ require an algorithm *coupling* nucleosynthesis and convective diffusion. Such an algorithm has been implemented in our code, but is very time-consuming. It has been applied to the calculation of one pulse, as described in Sect. 4.1, in order to evaluate the accuracy of the results derived from the simpler procedure.

Nuclear reaction rates are taken from Caughlan & Fowler (1988; CF88), except for the reactions listed in Appendix. New reaction rates of importance for the ^{19}F nucleosynthesis include $^{15}N(\alpha,\gamma)^{19}F$ (de Oliveira et al. 1995) and $^{18}O(\alpha,\gamma)^{22}Ne$ (Giesen et al. 1994). The new $^{15}N(\alpha,\gamma)^{19}F$ rate is slower than the CF88 one by a factor 1.5 to 50 in the temperature range $2 \leq T_8 \leq 3$ of interest here (T_8 is the temperature in units of 10^8 K). The impact of this change on the ^{19}F nucleosynthesis has been investigated by de Oliveira et al. (1995).

4 Model predictions

Three intermediate-mass stars are computed with (mass, metallicity) pairs of (3, 0.02), (3, 0.001) and (6, 0.02), referred to as M3Z02, M3Z001 and M6Z02, respectively.

Our models are computed from the pre-main sequence phase, when the star is on the Hayashi track with central temperatures less than 10^6 K. The structural and chemical evolution of the three stars are followed all the way up to the 13th, 15th and 11th pulse of the AGB phase for the M3Z02, M3Z001 and M6Z02 stars, respectively. A detailed description of the structural and chemical evolution of these stars can be found in Mowlavi (1995a). In the remaining part of this paper, we concentrate only on the fluorine production in the AGB phase.

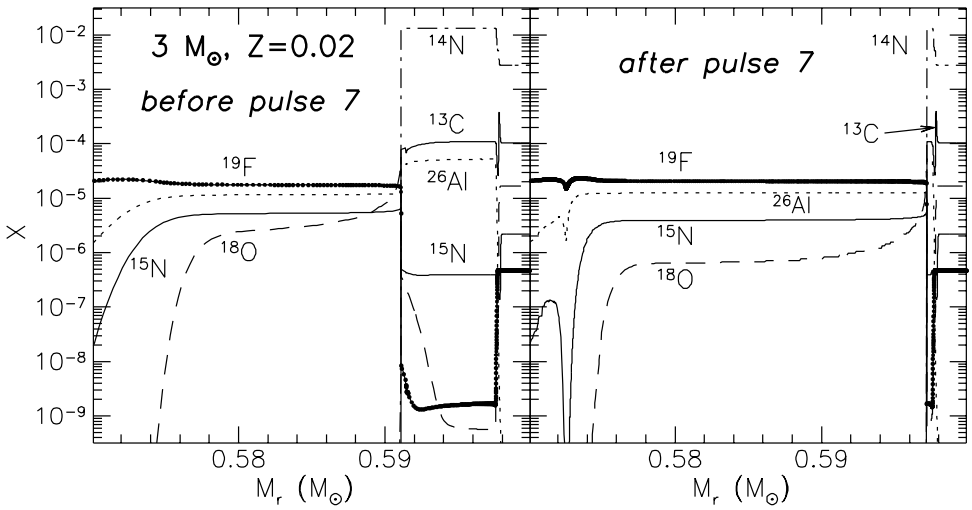

Figure 3: Abundance profiles before (left panel), and after (right panel) the 7th pulse of the $3\,M_\odot$, Z=0.02 star. Regions *a* and *b* defined in the text are readily identified on the left panel. In the left panel, the rapid drop of the ^{19}F abundance to the right of the plateau corresponds to the maximum outward extension of pulse 6, and marks the transition between regions *a* and *b*. The dots on the ^{19}F profiles correspond to the mesh distribution

4.1 The 3 $M_\odot$, $Z = 0.02$ case

The features governing the ^{19}F synthesis in relatively cool thermal pulses can be illustrated by considering the 6th and 7th pulses of the M3Z02 star. The location of the convective boundaries of these pulses is displayed in Fig. 2 as a function of time. The pulse duration, $\Delta t_{\rm pulse}$, is 182 and 159 y for the 6th and 7th pulse, respectively, and the maximum base temperature $T_{\rm pulse,b} = 239$ and $245\,10^6$ K, respectively. Defining the maximum inward and outward extensions of pulse n as $M_{p,b}^{(n)}$ and $M_{p,t}^{(n)}$, respectively, the overlap

$$r = \frac{M_{p,t}^{(6)} - M_{p,b}^{(7)}}{M_{p,t}^{(7)} - M_{p,b}^{(7)}}$$

between pulses 6 and 7 amounts to 0.753. Thus 75.3% of the mass of pulse 7 (defined as region *b* on Fig. 2, and extending from $M_r = 0.572$ to $0.591\,M_\odot$) is inherited from pulse 6, the remaining fraction (defined as region *a* on Fig. 2, and extending from $M_r = 0.591$ to $0.597\,M_\odot$) containing the ashes left behind by the hydrogen-burning shell. These two regions are readily identified on the left panel of Fig. 3, which displays the abundance profiles of ^{13}C, ^{14}N, ^{15}N, ^{18}O, ^{19}F and ^{26}Al before pulse 7. The drop in ^{15}N and ^{18}O observed at the bottom of region *b* translates the fact that α-capture reactions continue to operate on these nuclides in the hottest layers below pulse 6. A concomitant small hump in the fluorine abundance is also observed in these layers. On the other hand, the non-homogeneous profile exhibited by ^{18}O in the upper part of region *b* corresponds to the ^{18}O abundance frozen, in a given layer, at its value in the 6th pulse at the time the considered layer became radiative.

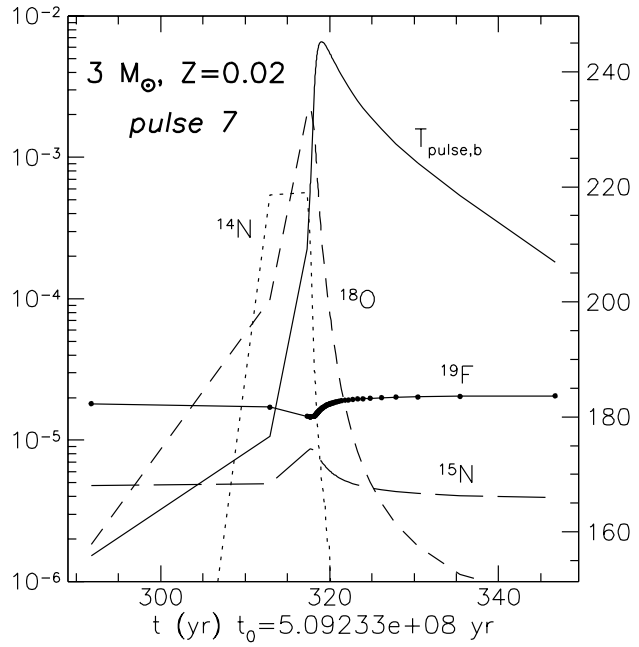

Figure 4: Evolution of the ^{14}N, ^{15}N, ^{18}O and ^{19}F mass fractions during the 7th pulse of the $3\,M_{\odot}$, Z=0.02 star. The evolution of the temperature at the base of the pulse is also shown (solid line), to be read on the right scale (in units of 10^6 K). The quantities are plotted every 4 to 6 models, resulting in a poor time-resolution for some species

The evolution of the abundances of several nuclides of interest during the 7th pulse is shown in Fig. 4. The ingestion of ^{14}N and the concomitant production of ^{18}O are clearly visible during the growing phase of the pulse. The ^{19}F abundance, on the other hand, first decreases slightly as the pulse grows into fluorine-depleted regions. It then increases as soon as $^{15}\mathrm{N}\,(\alpha\,,\gamma)\,^{19}\mathrm{F}$ starts operating. A net increase in the fluorine abundance at the end of the pulse, as compared to its value before the pulse, is clearly apparent on Figs. 3 and 4, even though the conversion of ^{15}N into ^{19}F has not been complete. It is noteworthy that such a net ^{19}F production has been possible *even though* the amount of ^{18}O inherited from the previous pulses is about ten times lower than the ^{19}F abundance level. In fact, ^{13}C and ^{14}N are not ingested instantaneously at the start of the pulse, but are instead mixed in progressively. The ingestion time scale is set by the rate of outward progression of the pulse convective tongue. This time scale turns out to be longer than the one for ^{18}O production. In other words, neutrons are released by $^{13}\mathrm{C}\,(\alpha\,,\mathrm{n})\,^{16}\mathrm{O}$ in presence of ^{18}O produced earlier in the pulse by $^{14}\mathrm{N}\,(\alpha\,,\gamma)\,^{18}\mathrm{F}\,(\beta^{+})^{18}\mathrm{O}$ (see Fig. 4).

The intershell mass fractions $X_{\rm out}$ of ^{15}N and ^{19}F at the end of each pulse are shown in Fig. 5 as a function of the pulse number. The fraction of ^{15}N converted into ^{19}F is low in the first pulses [3]. It is, however, an increasing function of the pulse number, i.e. of the maximum temperature reached at the base of the pulse. The dotted line in Fig. 5 represents

[3]The conversion of ^{15}N into ^{19}F was faster with the CF88 rate for $^{15}\mathrm{N}\,(\alpha\,,\gamma)\,^{19}\mathrm{F}$. We refer to de Oliveira et al. (1995) for a discussion of the impact of the new rate on ^{19}F production in thermal pulses

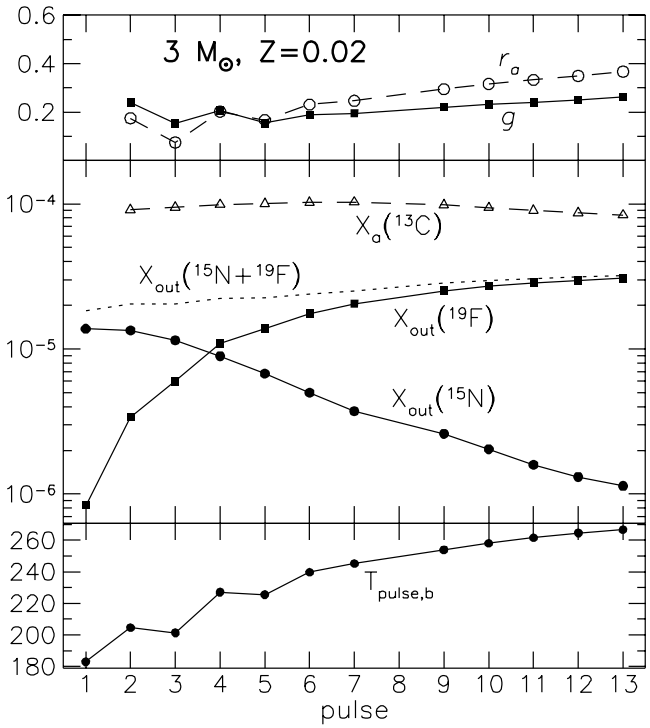

Figure 5: Various quantities in the $3\,M_\odot$, Z=0.02 star as a function of pulse number. *Lower panel*: Maximum temperature at the base of the thermal pulse; *Middle panel*: Intershell ^{15}N (filled circles), ^{19}F (filled squares) and ^{15}N+^{19}F (dotted line) mass fractions at the end of the pulse, as well as ^{13}C mass fraction averaged over region a as defined in Fig. 2 (open triangles); *Upper panel*: Efficiency factor g of fluorine production in the pulse (filled squares) and dilution factor r_a of the hydrogen-burning ashes into the pulse (open circles)

the maximum ^{19}F mass fraction that would result from the complete conversion of ^{15}N into ^{19}F. That limiting value is roughly constant with pulse number. In other words, the efficiency of ^{15}N production through the above-mentioned reactions is not very sensitive to the pulse temperature, at least when $T_{\rm pulse,b} < 260\,10^6$ K. The fraction of ^{15}N that can be converted into ^{19}F in these pulses *is* however sensitive to the pulse temperature (Fig. 5).

As already indicated in Sect. 2, the amount of ^{15}N that can be produced is limited by the available neutrons, i.e. by the available ^{13}C supply. The maximum efficiency would correspond to a situation where each neutron liberated by $^{13}\mathrm{C}\,(\alpha\,,\mathrm{n})\,^{16}\mathrm{O}$ produces a proton which is then captured by $^{18}\mathrm{O}\,(\mathrm{p}\,,\alpha)\,^{15}\mathrm{N}$. The actual efficiency can be derived from baryon number conservation, as expressed by the relation

$$g = \frac{\frac{19}{15}X_{\rm out}(^{15}{\rm N}) + X_{\rm out}(^{19}{\rm F}) - \frac{19}{15}X_{\rm in}(^{15}{\rm N}) - X_{\rm in}(^{19}{\rm F})}{\frac{19}{13}X_{\rm in}(^{13}{\rm C})}, \qquad (1)$$

where the subscript *in* refers to the intershell mass fractions averaged over region $a+b$ before the considered pulse, and the subscript *out* to the abundance at the end of the pulse. The average ^{13}C mass fraction injected in the pulse, $X_{\rm in}(^{13}{\rm C})$, results from the dilution into the

pulse of ^{13}C left behind by the hydrogen-burning shell [$X_a(^{13}\mathrm{C})$ in the middle panel of Fig. 5]. The dilution factor

$$r_a = M_a/(M_a + M_b), \tag{2}$$

where M_a and M_b are the masses of regions a and b, respectively (see Fig. 2), amounts to about 25% for the 7th pulse. The actual efficiency turns out to be around 20%, as seen in the upper panel of Fig. 5.

Another way of evaluating the efficiency is based on nuclear flux considerations. Leakage on the path from ^{13}C to ^{15}N first occurs from neutrons liberated by $^{13}\mathrm{C}\,(\alpha\,,\mathrm{n})\,^{16}\mathrm{O}$ and involved in (n,γ) rather than in (n,p) reactions. The main neutron poison in that respect is ^{56}Fe. The efficiency g_1 with which protons are liberated from a ^{13}C seed is

$$\begin{aligned} g_1 &= \frac{\sum\limits_{(\mathrm{n,p})} \sigma_{\mathrm{A,np}} Y_{\mathrm{in}}(^{\mathrm{A}}\mathrm{Z})}{\sum\limits^{*}_{\mathrm{n-capture}} \sigma_{\mathrm{A,n}} Y_{\mathrm{in}}(^{\mathrm{A}}\mathrm{Z})} \\ &\simeq \frac{\sigma_{14,\mathrm{np}} Y_{\mathrm{in}}(^{14}\mathrm{N}) + \sigma_{26,\mathrm{np}} \mathrm{Y}_{\mathrm{in}}(^{26}\mathrm{Al})}{\sigma_{14,\mathrm{np}} Y_{\mathrm{in}}(^{14}\mathrm{N}) + \sigma_{26,\mathrm{np}} \mathrm{Y}_{\mathrm{in}}(^{26}\mathrm{Al}) + \sigma_{56,\mathrm{n}} \mathrm{Y}_{\mathrm{in}}(^{56}\mathrm{Fe})}, \end{aligned} \tag{3}$$

where $Y(^{\mathrm{A}}\mathrm{Z}) = \mathrm{X}(^{\mathrm{A}}\mathrm{Z})/\mathrm{A}$ and σ stands for the Maxwellian-averaged neutron-capture cross section. The sum $\sum^*$ runs over all n-capture reactions except $^{12}\mathrm{C}\,(\mathrm{n}\,,\gamma)\,^{13}\mathrm{C}$, as this reaction replenishes ^{13}C. Since ^{14}N is only present in the hydrogen-burning ashes (region a; see Fig. 3), its abundance after dilution in the pulse is $X_{\mathrm{in}}(^{14}\mathrm{N}) = \mathrm{r_a X_a}(^{14}\mathrm{N})$, with $X_a(^{14}\mathrm{N}) = 10^{-2}$, X_a designating the mass fraction averaged over region a. A similar relation holds for ^{26}Al in the M3Z02 star, with $X_a(^{26}\mathrm{Al}) \sim 5\,10^{-5}$. On the contrary, $X_{\mathrm{in}}(^{56}\mathrm{Fe})$ is independent of r_a, as ^{56}Fe keeps its primordial abundance throughout the star. Therefore, as ^{56}Fe constitutes the main neutron poison competing with $^{14}\mathrm{N(n,p)}^{14}\mathrm{C}$ and $^{26}\mathrm{Al(n,p)}^{26}\mathrm{Mg}$, its importance will be comparatively larger, and thus g_1 smaller, for smaller dilution factors r_a. *The efficiency of fluorine production in the pulse is thus dependent on the pulse overlap factor* $r = 1 - r_a$, g_1 *increasing with decreasing* r. This is clearly seen on the upper panel of Fig. 5, which shows that the efficiency correlates well with the dilution factor. On the contrary, the efficiency is seen to be almost independent of the temperature, at least over the range $1.8 \leq T_8 \leq 2.5$. This is consistent with the fact that the Maxwellian-averaged rates for the neutron-capture reactions of interest are almost independent of temperature.

A second leakage in the fluorine production comes from protons captured by nuclides other than ^{18}O. The efficiency g_2 with which protons liberated by (n,p) reactions contribute to $^{18}\mathrm{O}\,(\mathrm{p}\,,\alpha)\,^{15}\mathrm{N}$ may be written

$$g_2 = \frac{\sigma_{18,\mathrm{p}\alpha} Y_{\mathrm{in}}(^{18}\mathrm{O})}{\sum\limits_{\mathrm{p-capture}} \sigma_{\mathrm{A,p}} Y_{\mathrm{in}}(^{\mathrm{A}}\mathrm{Z})}, \tag{4}$$

where the symbols are as in Eq. (3). The analysis of the reaction fluxes indicates that $g_2 \sim 0.90$ in the pulses of the M3Z02 star.

Finally, the efficiency of fluorine production can be decreased further by $^{19}\mathrm{F}\,(\mathrm{n}\,,\gamma)\,^{20}\mathrm{F}$ and/or $^{19}\mathrm{F}\,(\alpha\,,\mathrm{p})\,^{22}\mathrm{Ne}$. The n-capture reaction does not play an important role given the low neutron fluences encountered in our calculations. The α-capture reaction, on the other

hand, is not (yet) operating in the (still too cold) pulses encountered in the M3Z02 star. If $(1 - g_3)$ is the fraction of ^{19}F destroyed, the total efficiency g of fluorine production is given by $g = g_1 * g_2 * g_3$.

The maximum fluorine abundance that can be expected in the intershell region can now easily be estimated from the above considerations. Assuming that ^{15}N is fully converted into ^{19}F during the pulses (as is the case after a few pulses), the ^{19}F mass fraction at the end of pulse n is equal to

$$X_{\rm out}^{(n)}(^{19}{\rm F}) = (1 - {\rm r_a}){\rm X}_{\rm out}^{({\rm n}-1)}(^{19}{\rm F}) + {\rm r_a}\frac{19}{13}{\rm gX}_{\rm a}^{({\rm n})}(^{13}{\rm C}), \quad (5)$$

where the first term on the right-hand side represents the fluorine abundance inherited from the previous pulses, and the second term the amount of fluorine produced from the ^{13}C injected in the pulse. As fluorine builds up pulse after pulse, its abundance will reach an asymptotic value when $X_{\rm out}^{(n)} = X_{\rm out}^{(n-1)}$ (assuming a constant overlap factor). Equation (5) yields, in the asymptotic regime,

$$X_{\rm out}(^{19}{\rm F}) = \frac{19}{13}{\rm gX_a}(^{13}{\rm C}) \quad (6)$$

This value can easily be computed from the equilibrium ^{13}C mass fraction $X_a(^{13}{\rm C})$ resulting from the CNO cycles, and from the neutron balance expressed by Eq. (3). With $X_a(^{13}{\rm C}) \simeq 10^{-4}$ and $g \simeq 0.20$, this leads to $X_{\rm out}(^{19}{\rm F}) \simeq 3\,10^{-5}$, which is precisely the asymptotic value obtained in the M3Z02 star (Fig. 5).

The results presented above are obtained assuming instantaneous mixing in the convective zone (except for neutrons). This assumption is, however, not strictly valid for protons and in some cases ^{18}O, whose nuclear lifetimes may become shorter than the convective mixing time scale. The use of a very computer time-consuming algorithm coupling diffusion and nucleosynthesis (Sect. 3) does not lead, however, to significantly different ^{19}F abundances in a test run on the 7th pulse.

4.2 The 3 $M_\odot$, $Z = 0.001$ case

The evolution of the fluorine abundance in the $3\,{\rm M}_\odot$, Z=0.001 star is shown in Fig. 6 as a function of the pulse number. Several important differences exist as compared to the M3Z02 case:

i) The maximum fluorine abundance, corresponding to the complete transformation of ^{15}N into ^{19}F, is reached *much* faster in the M3Z001 star (after 3 pulses) than in the M3Z02 star (at least 10 pulses are needed). This is due to the higher temperatures reached in the pulses of the low-metallicity star.

ii) The efficiency of ^{19}F synthesis (upper panel of Fig. 6) during the first pulses is much larger than in the M3Z02 star ($g \sim 0.50$ as compared to 0.20). This is due to the combined effect of smaller overlap factors between successive pulses (see the discussion of Sect. 4.1) and of larger ^{26}Al/^{56}Fe abundance ratios left behind by the hydrogen-burning shell and ingested by the pulse. Arnould & Mowlavi (1993, see also Arnould et al. 1995) showed that the ^{26}Al abundance resulting from hydrogen burning sensitively depends upon the temperature, being maximum for temperatures around $T_6 \sim 70$. The temperature $T_{\rm HBS}$ in the hydrogen-burning

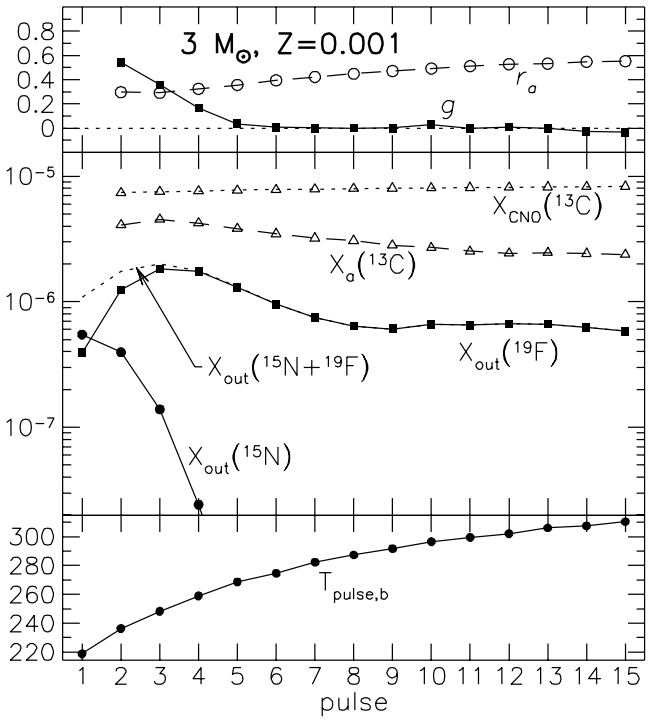

Figure 6: Same as Fig. 5, but for the $3\,M_\odot$, Z=0.001 star. In the middle panel, $X_{CNO}(^{13}C)$ corresponds to the ^{13}C mass fraction left behind by the hydrogen-burning shell. The difference between $X_{CNO}(^{13}C)$ and $X_a(^{13}C)$ is due to the interpulse ^{13}C burning

shell is indeed more favorable to ^{26}Al production in the M3Z001 star ($T_{HBS} = 73\,10^6$ K before the first pulse) than in the M3Z02 star ($T_{HBS} = 45\,10^6$ K before the first pulse). As a consequence, the ability of ^{14}N and ^{26}Al to compete with the neutron poisons is much higher during the first pulses of the M3Z001 star. In the second pulse of the M3Z001 star, about 10 and 50% of the neutrons liberated by $^{13}C\,(\alpha\,,n)\,^{16}O$ are captured by $^{14}N\,(n\,,p)\,^{14}C$ and $^{26}Al\,(n\,,p)\,^{26}Mg$, respectively.

The efficiency, however, rapidly decreases, and drops to zero after the 5th pulse. This results from two effects. First, the intershell ^{26}Al abundance decreases as the temperature of the hydrogen-burning shell exceeds $70\,10^6$ K. Secondly, the temperature in the He-rich layers is high enough for $^{13}C\,(\alpha\,,n)\,^{16}O$ to *destroy ^{13}C in the deep layers of region a during the interpulse period*. This is clearly seen on Fig. 7, which displays the abundance profiles before the 5th pulse of the M3Z001 star. As a consequence, the surviving ^{13}C is injected in the pulse at a time where the base temperature is close to its maximum. At these high temperatures, the destruction time scale of ^{14}N against α-capture becomes smaller than its injection rate in the pulse, so that its abundance decreases. Both effects drastically reduce the ability of ^{14}N and ^{26}Al to compete with ^{56}Fe for capturing neutrons, resulting in a drop of the efficiency of fluorine production within the thermal pulses.

iii) The interpulse ^{13}C burning leads to concomitant *^{15}N production in radiative layers*, as seen on Fig. 7. When injected in the pulse, this ^{15}N will *directly* produce ^{19}F through

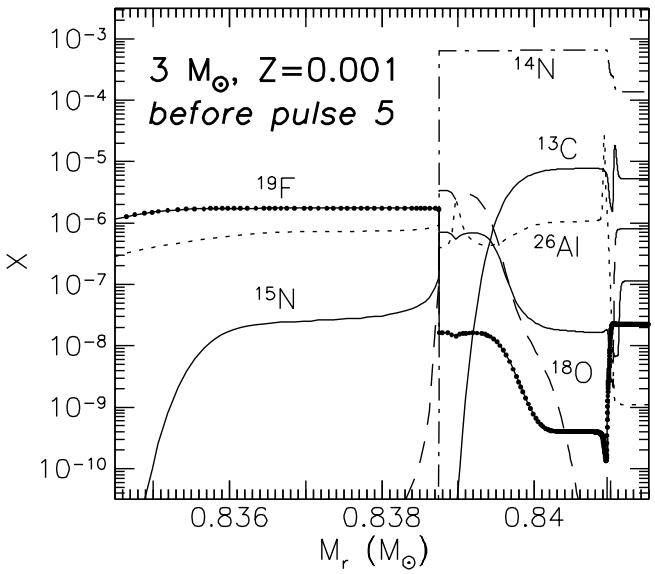

Figure 7: Same as Fig. 3, but for the 5th pulse of the $3\,M_\odot$, Z=0.001 star

$^{15}N\,(\alpha\,,\gamma)\,^{19}F$. Figure 8 shows how the different contributions to the after-pulse fluorine abundance vary with pulse number. In the early pulses, ^{15}N is produced from ^{13}C within the pulse, with an efficiency decreasing with the pulse number. The after-pulse fluorine abundance, resulting from the conversion of ^{15}N, reaches a maximum at pulse 3 and then decreases. From pulse 5 on, a substantial amount of ^{15}N is produced in region *a* during the interpulse period $[X_{\rm in,a}(^{15}N)]$, and represents, after injection in the pulse $[X_{\rm in}(^{15}N)]$, the main contribution to the after-pulse fluorine abundance. It is noteworthy that the F plateau reached with this radiative ^{15}N contribution is lower than the one that would have resulted had ^{15}N been synthesized in the pulse. This translates the fact that the efficiency $g_{rad}(\sim 0.09)$ of ^{15}N production in radiative layers is actually lower than in convective (cold) pulses. Indeed, in a radiative layer, the ^{18}O necessary to produce ^{15}N through $^{18}O\,(p\,,\alpha)\,^{15}N$ becomes available through $^{14}N\,(\alpha\,,\gamma)\,^{18}F\,(\beta^+)^{18}O$, only after a substantial amount of ^{13}C has already been burned. This results from the longer $^{14}N\,(\alpha\,,\gamma)\,^{18}F\,(\beta^+)^{18}O$ time scale as compared to the $^{13}C\,(\alpha\,,n)\,^{16}O$ one.

iv) Finally, fluorine destruction through $^{19}F\,(\alpha\,,p)\,^{22}Ne$ begins to operate when the temperature at the base of the pulse exceeds $300\,10^6$ K. This happens from the 13th pulse on in the M3Z001 star, and is clearly visible in Fig. 9, which shows the time evolution of the abundances in the 13th pulse. The efficiency of fluorine production decreases to *negative* values as a result of the fluorine destruction in the hot pulses of the low-metallicity star (Fig. 6, upper panel). The concomitant decrease of the after-pulse ^{19}F abundance is also observed in Fig. 6 (middle panel).

4.3 The 6 $M_\odot$, $Z = 0.02$ case

The situation for the M6Z02 star is qualitatively similar to that described for the M3Z001 star. The evolution of the after-pulse ^{19}F is simply delayed in the M6Z02 star as compared

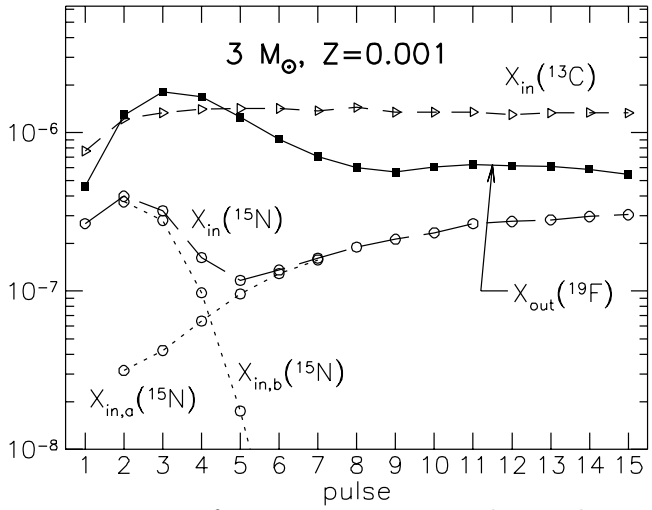

Figure 8: Mass fractions $X_{\rm in}$, averaged over the total mass covered by the pulse, of ^{13}C (open triangles) and ^{15}N (open circles, long-dashed line) before each pulse of the $3\,{\rm M}_\odot$, Z=0.001 star. The contributions from regions a and b (see Fig. 2), to the ^{15}N injected in the pulse are represented by open circles on doted lines, as labeled in the figure. The fluorine mass fraction $X_{\rm out}$ after each pulse, averaged over the mass of the pulse, is given by the filled squares

to the M3Z001 star, as a result of the lower pulse temperatures (namely $T_6 = 260$ and 290 in the 8th pulse of the M6Z02 and M3Z001 stars, respectively).

A specific feature of the M6Z02 star concerns however the temperatures at the base of the convective envelope, $T_{\rm env,b}$, which are *much* higher in the M6Z02 than in the M3Z02 and M3Z001 stars. At the first pulse, $T_{\rm env,b}$ amounts to 2.5, 6 and $50\,10^6$ K in the M3Z02, M3Z001 and M6Z02 stars, respectively, and to 4.6, 25 and $79\,10^6$ K at the 10th pulse, respectively. As a consequence, hydrogen burning occurs *in* the envelope of the M6Z02 star. This feature is known as hot-bottom burning (HBB).

The effect of hydrogen burning on fluorine depends on the temperature, as shown by Arnould & Mowlavi (1993). For $T_6 < 20$, fluorine is *produced* by $^{18}{\rm O}\,({\rm p}\,,\gamma)\,^{19}{\rm F}$, by a factor of up to 3 with respect to its solar-system abundance. At higher temperatures, it is essentially *destroyed* by $^{19}{\rm F}\,({\rm p}\,,\alpha)\,^{16}{\rm O}$. As a consequence of HBB, the ^{19}F abundance in the *envelope* of the M6Z02 star is thus expected to first increase, and then to decrease as the temperatures get higher. Figure 11 shows that the maximum envelope ^{19}F abundance is reached when $T_{\rm env,b} = 70\,10^6$ K [4], though the overabundance remains small ($[^{19}{\rm F}]=\log(X_{\rm env}(^{19}{\rm F})/{\rm X}_\odot(^{19}{\rm F})) = 0.07$). More important is the fluorine destruction in the envelope as the temperature exceeds $T_6 = 70$, which happens from the 4th pulse on in the M6Z02 star. Some fraction of the fluorine brought in the envelope by the third dredge-up (which we did not obtain in a self-consistent way in our models; see Sect. 5.2) would thus be destroyed as a result of the HBB.

[4]The "effective" temperature characterizing the nucleosynthesis in a convective zone is lower than the temperature at the base of that zone, because temperature-dependent reaction rates must be averaged over the whole convective region (see Sect. 3)

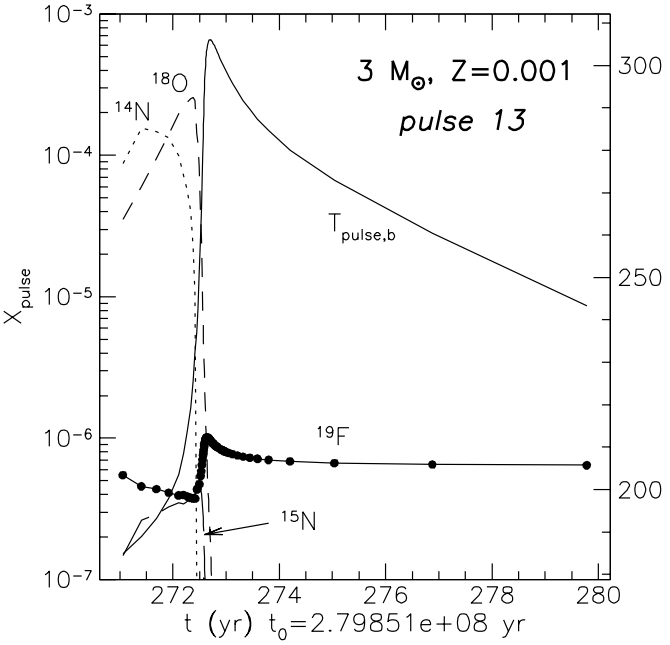

Figure 9: Same as Fig. 4, but for the 13th pulse of the $3\,M_{\odot}$, Z=0.001 star

5 Comparison with observations

Observations of fluorine abundances at the surface of giant stars are available only for stars with metallicities close to solar (Paper I), as displayed on Figs. 13 and 14. We thus restrict the comparison with observations to the M3Z02 and M6Z02 stars. Predictions for the low-metallicity star are nevertheless briefly presented in Sect. 5.3.

5.1 First and second dredge-ups

Before considering the fluorine production during the thermally-pulsing AGB phase, we address the question of surface ^{19}F alterations resulting from the first and second dredge-ups. They occur shortly after the end of the central hydrogen- and helium-burning phases, respectively, when the envelope engulfs the deep layers processed by hydrogen burning (the operation of the second dredge-up being restricted to stars with $M \lesssim 4\,M_{\odot}$).

The possibility that the surface fluorine abundance may be altered by the first or second dredge-ups is suggested by the observation of otherwise normal K and M giants exhibiting $^{19}F/^{16}O$ ratios significantly larger than solar (Fig. 13). Since these stars do not bear the typical signatures of AGB nucleosynthesis (e.g. overabundances of carbon and elements heavier than iron), fluorine production in the thermal pulses on the AGB cannot be invoked to account for their larger-than-solar ^{19}F abundances.

As mentioned in Sect. 4.3, fluorine is expected to be produced as well in hydrogen-burning layers when $T_6 < 20$ (Arnould & Mowlavi 1993, Arnould et al. 1995), and destroyed at higher temperatures. This gives rise to a peak in the ^{19}F profile, as shown in Fig. 12. The first dredge-up leads to a moderate increase (by about 0.05 dex) of the surface ^{19}F abundance in

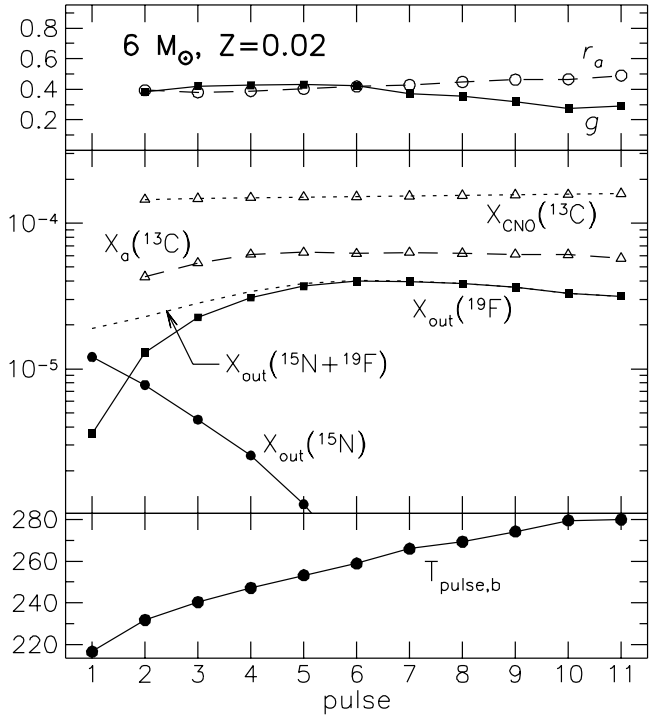

Figure 10: Same as Fig. 6, but for the $6\,M_\odot$, Z=0.02 star

the M3Z02 star, along with a decrease of the $^{12}C/^{16}O$ ratio (Fig. 13). No second dredge-up is experienced by this star. In the M6Z02 star instead, the temperatures in the hydrogen-burning layers are higher, resulting in a much thinner ^{19}F peak, so that the surface $^{19}F/^{16}O$ ratio is neither altered after the first, nor after the second dredge-up.

Clearly, the first and second dredge-ups in intermediate-mass stars cannot account for even the lowest F overabundances observed in M giants. This discrepancy may indicate that:
(i) the stellar fluorine abundances are systematically overestimated; or
(ii) the solar-system fluorine abundance is in error; or
(iii) the actual $^{19}F(p,\alpha)^{16}O$ reaction rate is slower than the intermediate rate provided by Kious (1990) and adopted in our calculations. In fact, that reaction rate is still largely uncertain in the temperature range of interest for hydrogen burning (see Arnould et al. 1995). To investigate the impact of these uncertainties on the first dredge-up predictions, a new evolutionary sequence has been computed up to the first dredge-up for the $3\,M_\odot$ star, adopting the lower limit for the $^{19}F(p,\alpha)^{16}O$ rate. The surface fluorine overabundance then reaches [F/O] = 0.13 dex (see Fig. 13). Although still on the low side of the observations, these predictions at least fall within the estimated ± 0.1 dex uncertainty on the observational data. The case of a solar-metallicity low-mass ($1.5\,M_\odot$) star has also been investigated with the low rate. The resulting surface F enhancement, also shown in Fig. 13, is much smaller than in the $3\,M_\odot$ star.

Clearly, the elucidation of the differences between the solar-system fluorine abundance and that of normal K and M giants remains a challenge for future studies. In Sect. 5.2,

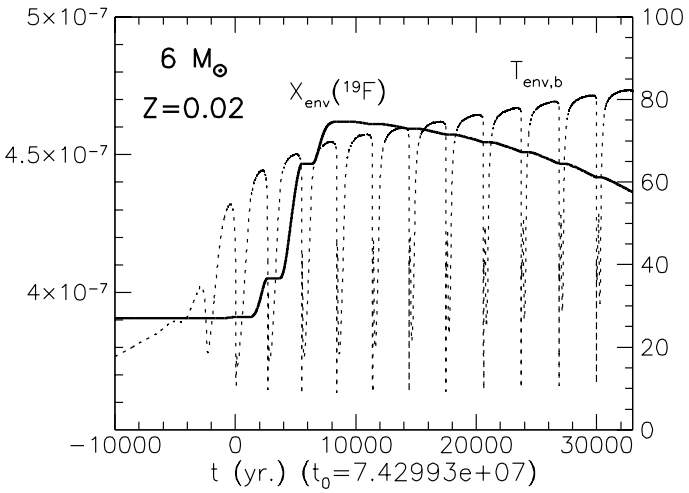

Figure 11: Fluorine abundance (thick solid line, corresponding to the left scale) in the envelope of the 6 $M_\odot$, Z=0.02 star, and temperature (dotted line, to be read on the right scale, in units of 10^6 K) at the base of the envelope. Time $t = 0$ corresponds to the occurrence of the first convective pulse. The temperature drop after each pulse results from the expansion, and concomitant cooling, of the hydrogen-rich layers following the thermal pulses

devoted to the analysis of the surface fluorine abundance resulting from the third dredge-up, we will therefore normalize our predictions in such a way that the pre-AGB ^{19}F abundance corresponds to the average value observed in solar-metallicity K and M giants (Fig. 14), whatever its origin might be.

5.2 Third dredge-up

After a pulse, the convective envelope extends inward and, in some cases, can penetrate the layers formerly involved in the thermal pulse. When this happens, the He-burning ashes, like ^{12}C and ^{19}F, are mixed in the convective envelope and brought to the surface. This process, called *third dredge-up*, accounts for the gradual transformation of a M star into a S and then C star along the AGB.

Though the very existence of S and C stars on the AGB supports the occurrence of such dredge-ups, our stellar models like most others fail in obtaining this process in a self-consistent way. No fully self-consistent comparison of the observed ^{19}F abundances with our predictions is thus possible.

Nevertheless, a comparison is attempted by parametrizing the dredge-ups. Two parameters need to be specified for that purpose: (i) the depth $\lambda = \Delta M_d/(M_a + M_b)$, where ΔM_d is the mass of matter from the pulse mixed into the convective envelope, and $(M_a + M_b)$ is the mass involved in the pulse (see Fig. 2); (ii) the pulse number $n_{\rm start}$ after which the third dredge-up first occurs. It is then assumed that dredge-ups with the same depth λ occur after each subsequent pulses. Though these free parameters introduce some uncertainties in our predictions, it was shown in Paper I (Eq. 1, Sect. 3.2) that the use of the (C/O, F/O) diagram strongly limits their impact. Actually, predictions almost independent of λ can be

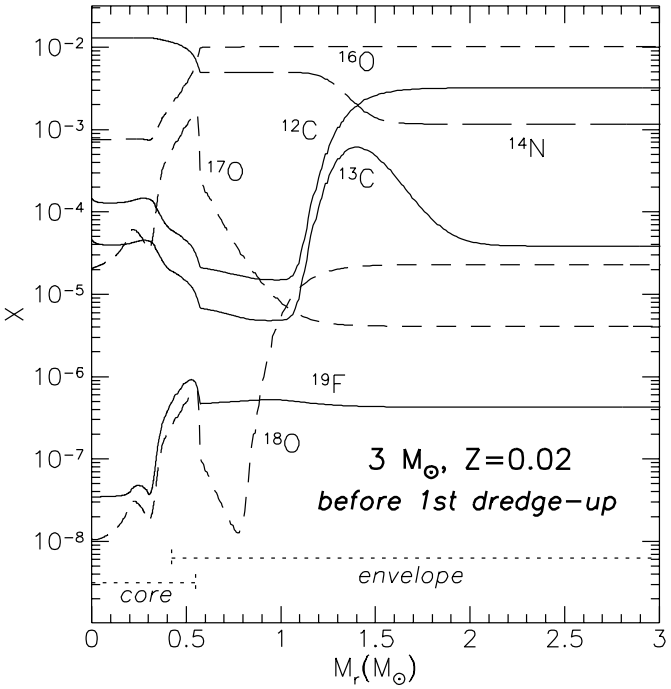

Figure 12: Mass fraction profiles of ^{12}C, ^{13}C, ^{14}N, ^{16}O, ^{17}O, ^{18}O and ^{19}F before the first dredge-up in the M3Z02 star. The maximum extension of the convective core during central hydrogen burning (labeled *core*), and the maximum inward penetration of the envelope during the red giant phase (labeled *envelope*) are indicated at the bottom of the figure

made by using this diagram.

The parametric dredge-up calculations start with the envelope abundances at pulse $n_{\rm start}$ as given by the detailed models. These envelope abundances are then modified after each subsequent pulse by mixing into the envelope the matter from the underlying layers, until a fraction λ of the ashes of the pulse has been dredged up. The abundance profiles are taken from the detailed model calculations. When HBB is taking place, as in the M6Z02 star (Sect. 4.3), its effect on the envelope abundances is incorporated in the parametric calculations by correcting the abundances by an amount equal to the relative variation obtained during the interpulse in the detailed calculations.

Figure 14 displays how the surface (C/O, F/O) ratios vary in the M3Z02 and M6Z02 stars as a result of the dredge-ups. As discussed in Sect. 5.1, our predictions are normalized in such a way that the surface F abundance prior to any dredge-up corresponds to the average F abundance observed in K and M giants. Predictions are given for $n_{\rm start} = 1$, 4 and 9, with a dredge-up depth $\lambda = 0.3$. In the case of the M3Z02 star, the surface fluorine overabundances at a given ^{12}C/^{16}O ratio are the largest for $n_{\rm start} = 9$ as expected, since the intershell fluorine abundance saturates from pulse 9 onwards in that star (Fig. 5). However, even in this case, our predictions can only account for the lowest observed fluorine overabundances. Predictions with $\lambda = 0.1$ lead to slopes in the (C/O, F/O) diagram similar to the ones obtained with

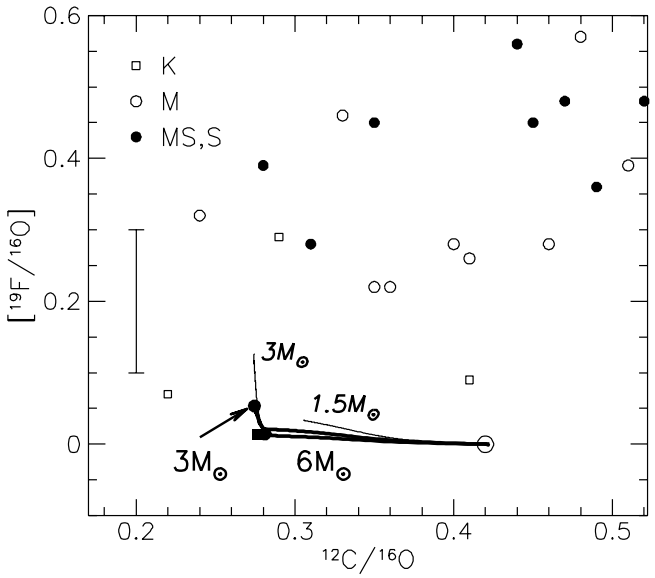

Figure 13: The ([^{19}F/^{16}O], ^{12}C/^{16}O) diagram, comparing the abundances observed in several classes of red giants from Paper I with our predictions for the first dredge-up (small filled circle along the solid lines) and the second dredge-up (small filled square along the solid lines). The thick lines correspond to the M3Z02 and M6Z02 stars, as labeled. The thin lines correspond to the first dredge-up predictions in 1.5 and 3 $M_\odot$ stars (italic labels) when the lower limit is taken for the ^{19}F (p , α) ^{16}O rate (Kious 1990), leading to the maximum ^{19}F production. Note that, unlike in Paper I, [^{19}F/^{16}O] = log(^{19}F/^{16}O)$_*$-log(^{19}F/^{16}O)$_\odot$, where subscripts $*$ and $\odot$ refer to stellar and solar abundances, respectively. The error bar corresponds to the estimated uncertainty on the observational data

$\lambda = 0.3$, and are not reported in Fig. 14 for clarity. The above conclusion is thus independent of the dredge-up parameter λ.

In the M6Z02 star, the dredge-ups do not lead to any significant F overabundances. This is due to the combined effects of the large dilution of the intershell ^{19}F in the massive envelope, and to HBB. Even though a slight increase in the surface F abundance is predicted during the early pulses, due mainly to fluorine production in the envelope itself (see Sect. 4.3), the operation of HBB at later pulses prevents any further increase. Moreover, by converting the envelope ^{12}C into ^{14}N, HBB leads to a decrease of the ^{12}C/^{16}O ratio in these massive AGB stars. Therefore, it is rather unlikely that the giants exhibiting large F/O ratios have experienced HBB, unless their F/O and C/O ratios prior to the onset of HBB were even larger than their present values. But according to the present models, massive AGB stars are not very efficient in increasing their surface F abundance even in the absence of HBB.

In this respect, WZ Cas is a puzzling case. This star is known to be super Li-rich (Denn, Luck & Lambert 1991, Abia et al. 1993), to have a low ^{12}C/^{13}C ratio, and to be enriched in s-process elements (Dominy 1985). Lithium is produced in the envelope of massive AGB stars (Sackmann & Boothroyd 1992) having temperatures $T_6 \gtrsim 50$ at their base (Mowlavi 1995b). As no large surface F overabundances are expected in these typical HBB conditions, the combination of large Li and F excesses at the surface of WZ Cas remains unexplained so

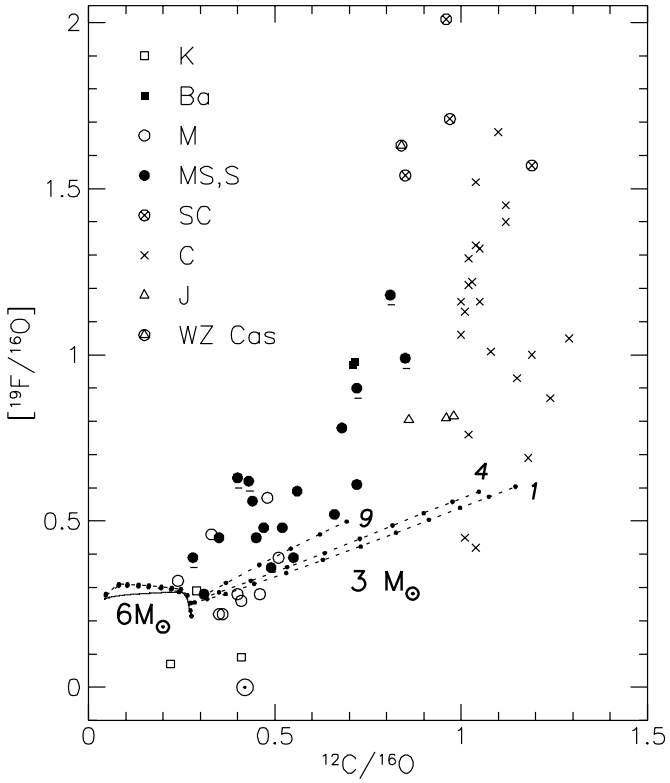

Figure 14: Same as Fig. 13, but for parametrized third dredge-up predictions. Dotted lines correspond to predictions with $\lambda = 0.3$ and $n_{\rm start} = 1$, 4 or 9, as defined in the text. Predictions are normalized in such a way that the surface F abundances prior to any third dredge-up correspond to the average F abundance observed in K and M giants. The solid line corresponds to the predictions for the M6Z02 star in the absence of third dredge-ups, reflecting the operation of HBB. Note that time is increasing from left to right (i.e. increasing C/O) in the M3Z02 tracks, but from right to left (i.e. decreasing C/O) in the M6Z02 ones. Underlined symbols denote stars with large N overabundances (see Paper I)

far. More observations of F abundances in super Li-rich stars are needed to know whether such a combination is common among these stars.

It is noteworthy that J stars (represented by open triangles in Fig. 14) exhibit rather large F overabundances. This class of giants is characterized by low ^{12}C/^{13}C ratios and no s-process overabundances (Lambert et al. 1986, Dominy 1985). Since their N abundance is not especially high, HBB alone seems inadequate to account for their peculiar abundances. The combination of low ^{12}C/^{13}C and high ^{19}F/^{16}O ratios is also puzzling in that respect, as the extensive hydrogen burning implied by the low ^{12}C/^{13}C ratio is also expected to destroy any pre-existing ^{19}F, unless hydrogen burning occurs at $T_6 < 20$ (Sect. 4.3).

In conclusion, the surface F abundances predicted for the intermediate-mass stars considered in this paper are in rather poor agreement with the observations displayed in Fig. 14. The predicted F abundances in the M3Z02 star are just able to account for the lowest observed overabundances (at a given C/O ratio). That conclusion is almost independent of

the parameters λ and $n_{\rm start}$. Actually, a better match to the observations would require to increase the ^{19}F/^{12}C ratio in the pulses by a factor of at least 10 (see Eq. 1 and Fig. 9 of Paper I), i.e. $X(^{19}{\rm F}) \gtrsim 2\,10^{-4}$ in the pulse. Equation (6) indicates that the maximum ^{19}F production level in the pulse is fixed by the available ^{13}C supply. For secondary ^{13}C supplied by the CNO cycles operating in the hydrogen-burning shell, $X_{\rm a}(^{13}{\rm C}) \sim 10^{-4}$, and the required ^{19}F production level is thus not achieved. That conclusion holds true for low-mass stars. It seems thus unavoidable that the most F-rich stars of Fig. 14 require a *primary* ^{13}C supply resulting possibly from a non-standard mixing of protons with the ^{12}C pocket left over by the pulse (e.g. Hollowell & Iben 1988). Since a similar need for a primary ^{13}C supply is in fact coming from the heavy-element overabundances observed in the same stars (Smith & Lambert 1990), one may expect the F and s-process overabundances to be correlated. The fact that the most F-rich stars are also the most heavy element-rich (Fig. 12 of Paper I) and the most N-rich (at a given C/O ratio; underlined symbols in Fig. 14) provides evidence for primary ^{13}C and ^{14}N supplies in these stars.

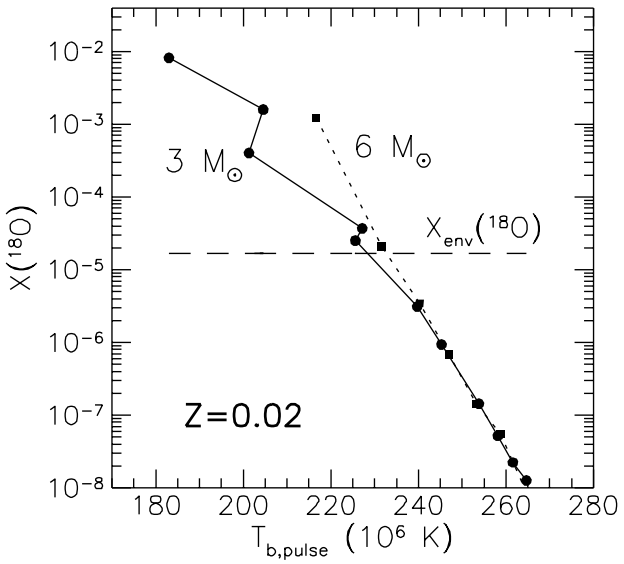

Figure 15: Intershell ^{18}O mass fractions after each pulse as a function of the maximum pulse temperature for the M3Z02 and M6Z02 stars. The dashed line corresponds to the surface ^{18}O abundance of the M3Z02 star prior to any third dredge-up

Another important constraint on the models comes from the surface ^{18}O abundance. In Paper II, large ^{18}O overabundances, not supported by the observations (Smith & Lambert 1990), were predicted to result from the third dredge-up. The new $^{18}{\rm O}\,(\alpha\,,\gamma)\,^{22}{\rm Ne}$ reaction rate (Giesen et al. 1994), which is faster than the CF88 rate used in Paper II by a factor of 100 at $T_6 = 160$, removes the discrepancy. Figure 15 displays the after-pulse ^{18}O intershell mass fraction as a function of the maximum pulse temperature, as well as the envelope abundance prior to any third dredge-up in the M3Z02 star. It is seen that the after-pulse ^{18}O abundance drops below the envelope abundance after the 4th pulse in the M3Z02 star. Therefore, in order to prevent surface ^{18}O overabundances, third dredge-ups should occur

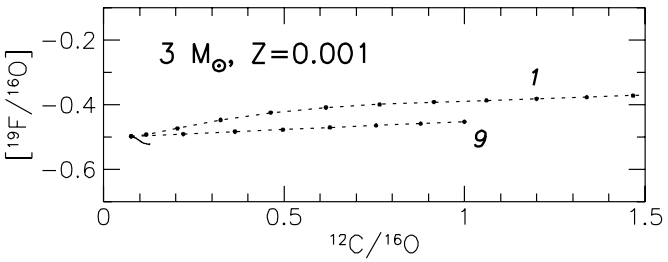

Figure 16: Same as Fig. 14, but for M3Z001 (see text). The scales are the same as in Fig. 14

after the 4th pulse in that star. The ^{18}O overabundance may however be more difficult to avoid in low-mass stars, where pulses are cooler.

5.3 Surface fluorine predictions in low-metallicity intermediate-mass stars

Surface fluorine abundances resulting from parametrized third dredge-ups are predicted for the M3Z001 star in a similar way as for the solar-metallicity stars (Sect. 5.2). It is important to note that these predictions for the low-metallicity star rely on several important assumptions regarding the *initial* envelope abundances. In our models, all initial abundances are taken equal to the solar-system values, scaled to the metallicity by the factor $Z/Z_{\odot}$. Such a scaling rule is justified for C and supposedly F, since [C/Fe] = 0 in unevolved disk stars (Edvardsson et al. 1993) and [F/Fe] $\sim$ 0 is suggested by the observations of the low-metallicity K giant α Boo (Arcturus, [Fe/H]=-0.6; see Paper I). It however does not hold for O, since it is well known that $[O/Fe] = -0.4\,[Fe/H]$ in the range $-1 \leq [Fe/H] \leq 0$ (e.g. Edvardsson et al. 1993). The initial ^{16}O abundance in the envelope of the M3Z001 star has been corrected correspondingly. With these assumptions, the starting point of the dredge-up tracks in the (^{12}C/^{16}O,[^{19}F/^{16}O]) diagram corresponds to (0.12,-0.52) (see Fig. 16).

As can be seen on Fig. 16, third dredge-up episodes in the M3Z001 star do not alter the surface fluorine abundance as strongly as in the solar-metallicity stars (Fig. 14). The increase in [^{19}F/^{16}O] with respect to its initial value is only 0.1 dex after a dozen of pulses, to be compared with as much as 0.4 dex in the solar-metallicity stars. The less steep slopes predicted in the (C/O, F/O) diagram for the M3Z001 star result from the combination of two effects: (i) the lower fluorine production efficiency in the hot pulses of the low-metallicity star as compared to the ones in the solar-metallicity cases (compare Figs. 5 and 6). The largest surface F overabundances in the M3Z001 star are therefore obtained when the dredge-ups occur after the early, cool pulses (compare tracks labeled *1* and *9* in Fig. 16); (ii) the primary nature of ^{12}C produced in the pulse, as compared to the secondary nature of ^{19}F in our models. This leads to ^{19}F/^{12}C ratios in the dredge-up material lower in low-metallicity stars than in solar-metallicity stars.

In conclusion, rather small F overabundances are expected in low-metallicity AGB stars, in the case that the fluorine production results from secondary ^{13}C only. Observations of F in low-metallicity giants would definitely be of great interest.

6 Conclusions

Detailed calculations of fluorine production have been performed in intermediate-mass stars with ($M/M_\odot$, Z) = (6, 0.02), (3, 0.02) and (3, 0.001). It is confirmed that ^{19}F *is* produced in pulses through $^{14}\mathrm{N}\,(\alpha\,,\gamma)\,^{18}\mathrm{F}\,(\beta^+)\,^{18}\mathrm{O}\,(\mathrm{p}\,,\alpha)\,^{15}\mathrm{N}\;\;(\alpha\,,\gamma)\,^{19}\mathrm{F}$, the necessary protons coming from (n,p) reactions with neutrons supplied by $^{13}\mathrm{C}\,(\alpha\,,\mathrm{n})\,^{16}\mathrm{O}$. Three different regimes of fluorine production can be identified:

1) In pulses with maximum base temperatures $T_6 \lesssim 260$, ^{15}N is produced *within the pulse*. For $T_6 \lesssim 220$, $^{15}\mathrm{N}\,(\alpha\,,\gamma)\,^{19}\mathrm{F}$ is however too slow to produce significant amounts of F. The maximum fluorine production is reached for $220 \lesssim T_6 \lesssim 260$, at a level limited by the ^{13}C supply and the efficiency g of ^{15}N production in the reaction chain starting at ^{13}C. Typical values for the efficiency are $g \sim 0.2$, and depend mainly upon the fraction of available neutrons involved in (n,p) reactions. ^{14}N and ^{26}Al are the main neutron-to-proton converters. The efficiency is found to depend also on the overlap factor between successive pulses.

2) In pulses with $T_6 \gtrsim 260$, the efficiency of ^{15}N production within the pulse drops dramatically. However, the temperature of the intershell region now gets high enough for ^{15}N to be produced *in radiative layers* during the interpulse period. When injected in the next pulse, that ^{15}N is entirely converted into ^{19}F by α-captures. The efficiency of ^{15}N production is lower in radiative layers than in a pulse ($g_{rad} \sim 0.1$). The intershell ^{13}C nuclei not burned during the interpulse period are ingested by the pulse close to the time of maximum pulse temperature. At these high temperatures, $^{14}\mathrm{N}\,(\alpha\,,\gamma)\,^{18}\mathrm{F}$ is fast enough to substantially reduce the number of ^{14}N seeds available to $^{14}\mathrm{N}\,(\mathrm{n}\,,\mathrm{p})\,^{14}\mathrm{C}$. The overall efficiency of ^{19}F production is thus lower in this regime than in regime 1.

3) In pulses with $T_6 \gtrsim 300$, $^{19}\mathrm{F}\,(\alpha\,,\mathrm{p})\,^{22}\mathrm{Ne}$ destroys ^{19}F.

The evolution of the after-pulse fluorine abundance $X_{\rm out}(^{19}\mathrm{F})$ in the intershell zone is dictated by the succession of these three regimes. It first increases during the first regime until a maximum value is reached, given by $X_{\rm out}(^{19}\mathrm{F}) = \frac{19}{13}\mathrm{gX}(^{13}\mathrm{C})$ (where $X(^{13}\mathrm{C})$ corresponds to the mass fraction of the available ^{13}C supply). During regime 2, $X_{\rm out}(^{19}\mathrm{F})$ drops until it reaches a plateau, with a level fixed by the efficiency g_{rad}. Finally, $X_{\rm out}(^{19}\mathrm{F})$ decreases steadily when regime 3 operates in the late pulses. *The optimum F production in AGB stars is achieved for thermal pulses having maximum base temperatures in the range* $220 \lesssim T_6 \lesssim 260$.

All three regimes have been encountered in the M3Z001 star where the pulse temperatures reach $T_6 = 260$ at the 4th pulse and 300 at the 13th. The plateau corresponding to the second regime is reached after 9 pulses in that star. The M6Z02 star enters regime 2 at the 7th pulse, while the M3Z02 star is still in regime 1 after 13 pulses.

Comparing our predictions of surface fluorine abundances with the observations leads to the following conclusions:

i) Neither the first nor the second dredge-ups can account for the observed discrepancy between the solar-system fluorine abundance and that of normal K and M giants.

ii) Our predictions of surface fluorine abundances resulting from parametrized third dredge-ups in intermediate-mass stars can only account for the lowest F overabundances observed in AGB stars. That conclusion is expected to hold true for low-mass stars when fluorine production results from secondary ^{13}C only. No concomitant ^{18}O overabundances are predicted

in our intermediate-mass stars, in agreement with the observations.

iii) The largest F overabundances observed in C stars call for an additional source of ^{13}C, of *primary* origin. A larger ^{13}C supply could account for the observed overabundances of both F *and* s-process elements. Detailed computations are however necessary to confirm that prediction.

iv) According to our models, massive AGB stars are not expected to build up large surface F abundances. Moreover, when operating at $T_6 \geq 70$, HBB leads to a gradual destruction of the envelope fluorine, thereby limiting the surface F overabundance that would result from the third dredge-up. The large fluorine overabundance reported for the super Li-rich star WZ Cas (where HBB is supposed to be operating) remains therefore unexplained so far.

v) Hot thermal pulses in intermediate-mass, *low-metallicity* AGB stars are less efficient in producing F. The lower ^{19}F/^{12}C ratio from these pulses does not lead to large F overabundances at the surface of these AGB stars. Any large overabundances that would be reported by (future) observations of low-metallicity stars, would require a primary source of ^{13}C.

References

[] Abia C., Boffin H.M.J., Isern J., Rebolo R., 1993, A&A 272, 455

[] Arnould M., Mowlavi N., 1993. In: Weiss W. W., Baglin, A. (eds.) Inside the Stars. (IAU Coll. 137). ASP Conf. Ser. 40, p. 310

[] Arnould M., Mowlavi N., Champagne A., 1995. In: Stellar Evolution: What Should Be Done; 32$^{\rm nd}$ Liège Int. Astroph. Coll. 1995, in press

[] Beer H., Voss F., Winters R.R., 1992, ApJS 80, 403

[] Caughlan G.R., Fowler W.A., 1988, Atomic Data and Nucl. Data Tables 40, 283 (CF88)

[] Charbonnel C., 1994, A&A 282, 811

[] Denn G.R., Luck R.E., Lambert D.L., 1991, ApJ 377, 657

[] de Oliveira F., Coc A., Aguer P., Angulo C., Bogaert G., Kiener J., Lefebvre A., Tatischeff V., Thibaud J.P., Fortier S., Maison J.M., Rosier L., Rotbard G., Vernotte J., Arnould M., Jorissen A., Mowlavi N., 1995, Nucl.Phys., in press

[] Dominy J.F., 1985, PASP 97, 1104

[] Edvardsson B., Andersen J., Gustafsson B., Lambert D.L., Nissen P.E., Tomkin J., 1993, A&A 252, 597

[] Forestini M., Paulus G., Arnould M., 1991, A&A 252, 597

[] Forestini M., Goriely S., Jorissen A., Arnould M., 1992, A&A 261, 157 (Paper II)

[] Giesen U., Browne C.P., Görres J., Ross J.G., Wiescher M., Azuma R.E., King J.D., Vise J.B., Buckby M., 1994, Nucl. Phys. A567, 146

[] Gilroy K.K., Brown J.A., 1991, ApJ 371, 578

[] Hollowell D., Iben I., 1988, ApJ 333, L25

[] Jorissen A., Smith V.V., Lambert D.L., 1992, A&A 261, 164 (Paper I)

[] Lambert D.L., Gustafsson B., Eriksson K., Hinkle K.H., 1986, ApJS 62, 373

[] Mowlavi N., 1995a, Ph.D. thesis, Université Libre de Bruxelles

[] Mowlavi N., 1995b. In: Crane Ph. (ed.) Proc. ESO/EIPC Workshop, The Light Element Abundances. Springer, p. 297

[] Prantzos N., Arnould M., Arcoragi J.P., 1987, ApJ 315, 209

[] Sackmann I.-J., Boothroyd A.I., 1992, ApJ 392, L71

[] Smith V.V., Lambert D.L. 1990, ApJS, 72, 387

[] Wallerstein G., Morell O., 1994, A&A 281, L37

[] Ziurys L. M., Apponi A. J., Phillips T. G., 1994, ApJ 433, 729

Appendix: references to nuclear reaction rates

This appendix provides the references for the reaction rates used in the present study when different from CF88 or from Beer et al. (1992, for neutron-capture reactions). Tables A1, A2 and A3 refer to proton-, neutron- and α-capture reactions, respectively. The Hauser-Feshbach method, implemented in the SMOKER code (Thielemann, Arnould & Truran 1987), has been used to derive the reaction rates for proton captures on ^{31}Si, ^{32}Si, ^{31}P, ^{32}P, ^{33}P, ^{32}S, ^{33}S and ^{34}S, not listed in Table A1.

References to tables

Almeida J., Käppeler F., 1983, ApJ 265, 417

Berheide M., Rolfs C., Schroeder U., Trautvetter H.P., 1993, Z.Phys.A 343, 483

Caughlan G.R., Fowler W.A., Harris M.J., Zimmerman B.A., 1985, Atom. Data Nucl. Data Tables 32, 197

Champagne A.E., Cella C.H., Kouzes R.T., Lowry M.M., Magnus P.V., Smith M.S., Mao Z.Q., 1988, Nucl. Phys. A487, 433

Champagne A.E., Brown B.A., Sherr R., 1993, Nucl.Phys. A556, 123

Decrock P., Delbar Th., Duhamel P., Galster W., Huyse M., Leleux P., Licot I., Liénard E., Lipnik P., Loiselet M., Michotte C., Ryckewaert G., Van Duppen P., Vanhorenbeeck J., Vervier J., 1991, Phys. Rev. Lett. 67, 808

Descouvemont P., Baraffe I., 1990, Nucl.Phys. A514, 66

de Oliveira F., Coc A., Aguer P., Angulo C., Bogaert G., Kiener J., Lefebvre A., Tatischeff V., Thibaud J.P., Fortier S., Maison J.M., Rosier L., Rotbard G., Vernotte J., Arnould M., Jorissen A., Mowlavi N., 1995, submitted to Nucl. Phys.

Drotleff H.W., Denker A., Knee H., Soine M., Wolf G., Hammer J.W., Greife U., Rolfs C., Trautvetter H.P., 1993, ApJ 414, 735

Fowler W.A., Caughlan G.R., Zimmerman B.A., 1967, ARA&A 5, 525 (FCZ67)

Funck C., Langanke K., 1989, ApJ 344, 46

Gai M., Keddy R., Bromley D.A., Olness J.W., Warburton E.K., 1987, Phys. Rev. C36, 1256

Table A1: References for proton-capture reaction rates, if different from CF88

^{11}C (p , γ) ^{12}N (β^+) ^{12}C	Descouvemont & Baraffe 1990
^{13}N (p , γ) ^{14}O (β^+) ^{14}N	Decrock et al. 1991
^{14}C (p , γ) ^{15}N	Wiescher et al. 1990
^{17}O (p , α) ^{14}N	Berheide et al. 1993[a]
^{17}O (p , γ) ^{18}F	Berheide et al. 1993[a]
^{19}F (p , α) ^{16}O	Kious 1990
^{21}Ne (p , γ) ^{22}Na	Görres et al. 1982, Görres et al. 1983
^{22}Ne (p , γ) ^{23}Na	Görres et al. 1983
^{22}Na (p , γ) ^{23}Mg (β^+) ^{23}Na	Seuthe et al. 1990[b]
^{23}Na (p , γ) ^{24}Mg	CF88 + Görres et al. 1989[c]
^{25}Mg (p , γ) ^{26}Al^{g}	Iliadis et al. 1990[d]
^{25}Mg (p , γ) ^{26}Al^{i}	Iliadis et al. 1990[d]
^{26}Mg (p , γ) ^{27}Al	Iliadis et al. 1990[d]
^{26}Al^{g} (p , γ) ^{27}Si (β^+) ^{27}Al	Champagne et al. 1993[a]
^{27}Al (p , γ) ^{28}Si	Timmermann et al. 1988[a]
^{27}Al (p , α) ^{24}Mg	Timmermann et al. 1988 + Champagne et al. 1988[e,a]
^{28}Si (p , γ) ^{29}P (β^+) ^{29}Si	Graff et al. 1990
^{32}S (p , γ) ^{33}Cl (β^+) ^{33}S	Iliadis et al. 1992

[a] Geometric average between lower and upper limits

[b] Resonance at 70 keV from Berheide et al. (1993), plugged in expression from Landré et al. (1989) with f_1=f_2=1

[c] Resonant contributions from Görres et al. (1989)

[d] Geometric average between lower and upper limits for $T_9 > 0.01$

[e] Resonant contributions from Champagne et al. (1988)

Table A2: References for neutron-capture reaction rates, if different from Beer, Voss & Winters (1992)

$^{12}\mathrm{C}\,(\mathrm{n}\,,\gamma)\,^{13}\mathrm{C}$	Ohsaki et al. 1994
$^{13}\mathrm{C}\,(\mathrm{n}\,,\gamma)\,^{14}\mathrm{C}$	Raman et al. 1990
$^{13}\mathrm{N}\,(\mathrm{n}\,,\mathrm{p})\,^{13}\mathrm{C}$	CF88 (reverse)
$^{14}\mathrm{N}\,(\mathrm{n}\,,\mathrm{p})\,^{14}\mathrm{C}$	Koehler & O'Brien 1989
$^{15}\mathrm{N}\,(\mathrm{n}\,,\gamma)\,^{16}\mathrm{N}\,(\beta^-)\,^{16}\mathrm{O}$	FCZ67
$^{15}\mathrm{O}\,(\mathrm{n}\,,\mathrm{p})\,^{15}\mathrm{N}$	CF88 (reverse)
$^{17}\mathrm{O}\,(\mathrm{n}\,,\gamma)\,^{18}\mathrm{O}$	Wagoner 1969
$^{17}\mathrm{O}\,(\mathrm{n}\,,\alpha)\,^{14}\mathrm{C}$	Schatz et al. 1993
$^{18}\mathrm{O}\,(\mathrm{n}\,,\gamma)\,^{19}\mathrm{O}\,(\beta^-)\,^{19}\mathrm{F}$	Rauscher et al. 1994
$^{18}\mathrm{F}\,(\mathrm{n}\,,\alpha)\,^{15}\mathrm{N}$	Thibaud 1989
$^{18}\mathrm{F}\,(\mathrm{n}\,,\mathrm{p})\,^{18}\mathrm{O}$	Thibaud 1989
$^{21}\mathrm{Ne}\,(\mathrm{n}\,,\gamma)\,^{22}\mathrm{Ne}$	Almeida & Käppeler 1983
$^{26}\mathrm{Al}^{\mathrm{g}}\,(\mathrm{n}\,,\gamma)\,^{27}\mathrm{Al}$	WFHZ78
$^{26}\mathrm{Al}^{\mathrm{g}}\,(\mathrm{n}\,,\mathrm{p})\,^{26}\mathrm{Mg}$	CF88
$^{26}\mathrm{Al}^{\mathrm{g}}\,(\mathrm{n}\,,\alpha)\,^{23}\mathrm{Na}$	CF88
$^{26}\mathrm{Al}^{\mathrm{i}}\,(\mathrm{n}\,,\gamma)\,^{27}\mathrm{Al}$	WFHZ78
$^{26}\mathrm{Al}^{\mathrm{i}}\,(\mathrm{n}\,,\alpha)\,^{23}\mathrm{Na}$	CF88
$^{26}\mathrm{Al}^{\mathrm{i}}\,(\mathrm{n}\,,\mathrm{p})\,^{26}\mathrm{Mg}$	CF88
$^{31}\mathrm{Si}\,(\mathrm{n}\,,\gamma)\,^{32}\mathrm{Si}$	SMOKER
$^{32}\mathrm{Si}\,(\mathrm{n}\,,\gamma)\,^{33}\mathrm{Si}\,(\beta^-)\,^{33}\mathrm{P}$	SMOKER
$^{32}\mathrm{P}\,(\mathrm{n}\,,\gamma)\,^{33}\mathrm{P}$	SMOKER
$^{32}\mathrm{P}\,(\mathrm{n}\,,\mathrm{p})\,^{32}\mathrm{Si}$	SMOKER
$^{33}\mathrm{P}\,(\mathrm{n}\,,\beta^-)\,^{34}\mathrm{S}$	SMOKER
$^{33}\mathrm{S}\,(\mathrm{n}\,,\mathrm{p})\,^{33}\mathrm{P}$	SMOKER
$^{33}\mathrm{S}\,(\mathrm{n}\,,\alpha)\,^{30}\mathrm{Si}$	Wagemans et al. 1987

Table A3: References for α-capture reaction rates, if different from CF88

$^{12}\mathrm{C}\,(\alpha\,,\gamma)\,^{16}\mathrm{O}$	Caughlan et al. 1985
$^{13}\mathrm{C}\,(\alpha\,,\mathrm{n})\,^{16}\mathrm{O}$	Drotleff et al. 1993
$^{14}\mathrm{C}\,(\alpha\,,\gamma)\,^{18}\mathrm{O}$	Hashimoto et al. 1986, Gai et al. 1987, Funck & Langanke 1989
$^{15}\mathrm{N}\,(\alpha\,,\gamma)\,^{19}\mathrm{F}$	de Oliveira et al. 1995
$^{18}\mathrm{O}\,(\alpha\,,\gamma)\,^{22}\mathrm{Ne}$	Giesen et al. 1994
$^{22}\mathrm{Ne}\,(\alpha\,,\mathrm{n})\,^{25}\mathrm{Mg}$	Drotleff et al. 1993
$^{22}\mathrm{Ne}\,(\alpha\,,\gamma)\,^{26}\mathrm{Mg}$	Drotleff et al. 1992, priv. comm.

Giesen U., Browne C.P., Görres J., Ross J.G., Wiescher M., Azuma R.E., King J.D., Vise J.B., Buckby M., 1994, Nucl. Phys. A567, 146
Görres J., Rolfs C., Schmalbrock P., Trautvetter H.P., Keinonen J., 1982, Nucl.Phys. A385, 57
Görres J., Becker H.W., Buchmann L., Rolfs C., Schmalbrock P., Trautvetter H.P., Vlieks A., Hammer J.W., Donoghue T.R., 1983, Nucl.Phys. A408, 372
Görres J., Wiescher M., Rolfs C., 1989, ApJ 343, 365
Graff S., Görres J., Wiescher M., Azuma R.E., King J., Vise J., Hardie G.H., Wang T.R., 1990, Nucl. Phys. A510, 346
Hashimoto M., Nomoto K., Arai K., Kaminisi K., 1986, ApJ 307, 687
Iliadis Ch., Schange Th., Rolfs C., Schroeder U., Somorjai E., Trautvetter H.P., Wolke K., Endt P.M., Kikstra S.W., Champagne A.E., Arnould M., Paulus G., 1990, Nucl.Phys. A512, 509
Iliadis C., Giesen U., Görres J., Wiescher M., Graff S.M., Azuma R.E., Barnes C.A., 1992, Nucl.Phys. A539, 97
Kious 1990, Ph.D. thesis, Orsay
Koehler P.E., O'Brien 1989, Phys. Rev. C39, 1655
Landré V., Aguer P., Bogaert G., Lefebvre A., Thibaud J.P., Fortier S., Maison J.M., Vernotte J., 1989, Phys.Rev. C40, 1972
Ohsaki T., Nagai Y., Igashira M., Shima T., Takeda K., Seino S., Irie T., 1994, ApJ 422, 912
Raman S., Igashira M., Dozono Y., Kitazawa H., Mizumoto M., Lynn J.E., 1990, Phys.Rev. C41, 458
Rauscher Th., Applegate J.H., Cowan J.J., Thielemann F.-K., Wiescher M., 1994, ApJ 429, 499
Schatz H., Käppeler F., Koehler P.E., Wiescher M., Trautvetter H.P., 1993, ApJ 413, 750
Seuthe S., Rolfs C., Schroeder U., Schulte W.H., Somorjai E., Trautvetter H.P., Waanders, F.B., Kavanagh R.W., Ravn H., Arnould M., Paulus G., 1990, Nucl. Phys. A514, 471
Thibaud J.P., 1989, personal comm.
Thielemann F.-K., Arnould M., Truran J.W., 1986. In: Vangioni-Flam E., Audouze J., Cassé M., Chièze J.P., Tran Thanh Van J. (eds.) Advances in Nuclear Astrophysics. Ed. Frontières, Gif-sur-Yvette, p. 525
Timmermann R., Becker H.W., Rolfs C., Schroeder U., Trautvetter H.P., 1988, Nucl.Phys. A477, 105
Wagemans C., Weigmann H., Barthelemy R., 1987, Nucl.Phys. A469, 497
Wagoner R.W., 1969, ApJS 18, 247
Wiescher M., Görres J., Thielemann F.-K., 1990, ApJ 363, 340
Woosley S.E., Fowler W.A., Holmes J.A., Zimmerman B.A., 1978, Atomic Data Nucl. Data Tables 22, 371 (WFHZ78)